

Contact between rough rock surfaces using a dual mortar method

Cyrill von Planta¹, Daniel Vogler², Patrick Zulian¹, Martin O. Saar², and Rolf Krause¹

¹Università della Svizzera Italiana, Institute of Computational Science, Lugano, Switzerland

²ETH Zurich, Geothermal Energy and Geofluids Group, Institute of Geophysics, Zurich, Switzerland

September 6, 2019

Abstract

The mechanical behavior of fractures in solids, such as rocks, has strong implications for reservoir engineering applications. Deformations, and the corresponding change in solid contact area and aperture field, impact rock fracture stiffness and permeability thus altering the reservoir properties significantly. Simulating contact between fractures is numerically difficult as the non-penetration constraints lead to a nonlinear problem and the surface meshes of the solid bodies on the opposing fracture sides may be non-matching. Furthermore, the challenging geometry of the arising constraints requires to solve the problem in several iterations, adjusting the constraints in each one. Here we present a novel discrete implementation of a dual mortar method and a non-smooth SQP solver, suitable for parallel computing, and apply it to a two body contact problem consisting of realistic rock fracture geometries from the Grimsel underground laboratory in Switzerland. The contributions of this article are: 1) a novel, parallel implementation of a dual mortar method and non-smooth SQP method, 2) realistic rock geometries with rough surfaces, and 3) numerical examples, which prove that the dual mortar method is capable of replicating the nonlinear closure behavior of fractures, observed in laboratory experiments.

Keywords— contact mechanics, geomechanics, fracture, contact, mortar

1 Introduction

Mechanical contact of rough surfaces of fractures or faults along discontinuities in the rock mass is of significant importance in reservoir engineering applications, such as

enhanced geothermal systems (EGS) or CO₂ sequestration [1, 38]. The mechanical contact determines the normal and the shear compliances of rock fractures, which govern the geomechanical reservoir behavior and thereby influence economical efficiency and risk (e.g., induced seismic hazards or CO₂ leakage) of the reservoir application in question [28]. The mechanical behavior of rock fractures has therefore been studied extensively, with many studies focusing on surface topography [4, 51, 44] and the influence of surface topography on the mechanical behavior of the fracture [4, 33, 17, 27, 37, 43].

Specifically, surface topographies determine the contact area distribution of fractures for given loading conditions, and are thus crucial, when investigating fracture strengths in normal or shear directions. As a fracture is exposed to mechanical loading normal to the fracture, or loading is increased, fracture closure and load exhibit a non-linear relationship, with fracture closure increments becoming smaller with increasing load increments and displaying convergent behavior [4, 27, 51, 41, 43, 20]. This non-linear closure behavior of fractures can be attributed to the increase in contact area with fracture closure, which increases the fracture stiffness.

The described rock fracture surface topographies are complex, with characteristic features on the sub-millimeter scale [44]. Therefore, computing the contact and deformation of two such fracture surfaces constitute a two- or multi-body contact problem, a problem class that even in the standard finite element (FEM) setting with linearized contact, still poses a significant computational challenge to this day. This is the case for two reasons: First, the formulation of the non-penetration condition itself is non-trivial as the bodies in consideration normally have non-matching triangulations at the contact boundary. Secondly, the non-penetration condition at the a priori unknown contact zone between the bodies constrains the solution space of possible displacements, thereby introducing a nonlinearity. Simulation tools that resolve small-scale roughnesses, while allowing computation of contact stresses and stress variations in the rock mass, are rare. Most analytical or numerical studies at the laboratory or reservoir scale rely on simplifying assumptions and regularizations, such as averaging asperity scale processes with an empirical relationship, reduction to two dimensions, using variants of boundary element methods, not modeling explicitly the mechanical contact between two surfaces, treating the surfaces as two parallel plates, using penalty methods or only matching triangulations at the surface [4, 30, 8, 29, 11, 13, 35, 34, 26, 9].

In this work, we present a new parallel implementation of an approach that does not require any of the previously mentioned assumptions. The approach is conventional in as much as we employ linear elasticity and linearized contact conditions in the strong formulation [18]. However, when discretizing with finite elements, we use non-uniform meshes with non-matching surface meshes at the contact boundary and then employ a mortar projection to resolve the contact conditions across the non-matching contact surfaces. We follow [50] in that we use a mortar projection with dual Lagrange multipliers and apply a change of basis transform to the system, to effectively transform the two-body problem into a one-body problem. The formulation and discretization rest on a solid theoretical basis with proven numerical stability (see [6, 5, 49, 50] and references cited therein) and can be extended to also include friction [22] and multigrid acceleration for the solution of the constrained system [50, 12, 22]. For rough rock surfaces, our mortar technique is particularly useful, since we have complex, non-matching triangulations at the contact boundary (see Figure 1) and an unknown contact zone. Still, we want to obtain accurate three-dimensional representations of a fracture with contact areas to model fluid flow in fractures. For this, penalty-based approaches are at a disadvantage, as the solution can be distorted by over-closure or

additional convergence problems result from large penalty parameters. In the mortar case, the non penetration condition is enforced locally in a weak sense. Thus, while locally some interpenetration is possible, the discretization error depends on the local mesh size and can, if needed, be reduced at will through local refinement.

The use of this mortar technique has previously been hindered by the absence of an efficient way to compute the projection operator. The assembly of the operator requires the detection of intersections between the non-matching surface meshes. This is a complex task in parallel, as the portions of the intersecting meshes might reside on different compute nodes. To this end we use the relatively recently introduced MOONolith library [24] together with libMesh [19]. This, and the reliance on a finite element formulation, makes it feasible to apply the method to a wide range of problems, since the method can be incorporated into the vast number of available finite element software packages. Here, we combine the projection operator with custom components from the MOOSE framework [14] and PETSc [3, 2] to conduct our numerical experiments.

So far, only a few studies have applied dual mortar approaches for geophysics problems [39, 48], the focus being on macro scale problems with smooth surfaces. This article on the other hand focuses on the contact between rough surfaces at the micro scale, with non-vanishing initial gaps. To ensure a thorough introduction, we will emphasize the fundamentals of the dual mortar method, and not focus on the specifics of the implementation, which is available online.

This paper is organized as follows. In Section 2, we formulate the two-body contact problem. Then, we introduce the mortar projection and its discrete assembly, followed by the change of basis transformations and solution method to solve the resulting system. In Section 3, we show the characteristic boundary stresses from Hertzian contact and simulations of rough fractures, subjected to increased normal loads, which exhibit the characteristic nonlinear closing behavior of a fracture under increased normal stress.

2 Methods

In this section we introduce the dual mortar approach and the basis transformations needed to solve the two-body contact problem. An example for two-body contact on non matching grids is shown in Figure 1, where the mesh discretization on the fracture surface is shown for a cylindrical specimen with a fracture normal to the cylinder axis in the center.

The dual mortar approach for multibody contact problems is by now a thoroughly studied subject (see [49, 50, 12] and references cited therein). However, we believe that these formulations are still not well known in the geophysics community and we will therefore lay a strong emphasis on the formulation of the contact conditions, the dual mortar approach and the change of basis of the overall system. In particular, we would like to point the readers' attention to the successive metamorphosis of the non-penetration condition from a strong (Eq. 9) to a weak (Eq. 18) and, finally, using the mortar operator, to a discrete form (Eq. 25).

2.1 Contact formulation

For the formulation of the contact problem, we try to be as close as possible to the formulation and notation in [50, 12] and we refer the reader to these articles, and the

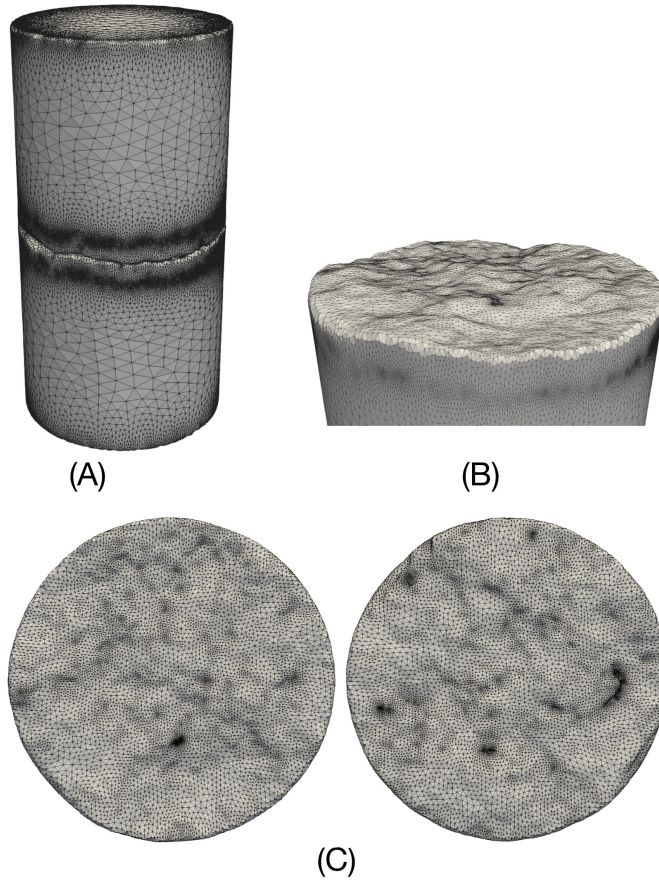


Figure 1: Mesh used for the numerical simulations with: A) The two specimen halves, which are separated by the fracture; B) The rough fracture surface of the lower specimen half; C) Normal view of the two non-matching meshes of the fracture surfaces.

references cited therein, for a more in-depth introduction.

We consider a master body $\Omega^m \subset \mathbb{R}^3$ and a slave body $\Omega^s \subset \mathbb{R}^3$. The choice, which body takes which role is arbitrary. We use the superscript $\alpha \in \{m, s\}$ for definitions that apply for both the master and the slave body. For example, the boundary Γ^α , $\alpha \in \{m, s\}$, of each body consists of three non overlapping parts: of a Neumann boundary Γ_N^α , a Dirichlet boundary Γ_D^α and a boundary Γ_C^α , where the possible contact occurs. Conversely we omit it, when we denote the union of master and slave body, i.e. $\Omega = \Omega^m \cup \Omega^s$ and so on. The displacement field on the bodies $u := [u^m, u^s]$ is separated into displacements on the master and slave body, respectively (see also Fig. 2). The material of Ω^α is considered to be linear elastic. By enforcing the summation convention on repeating indices from 1 to 3, Hooke's tensor $(E_{ijml}^\alpha)^3$, $1 \leq i, j, l, m \leq 3$ is used to formulate the stresses σ given by Hooke's law, using the index $_{,j}$ to abbreviate derivatives with respect to x_j :

$$\sigma_{ij}(u^\alpha) = E_{ijml}^\alpha u_{l,m}^\alpha. \quad (1)$$

We assume that a bijective mapping $\Phi : \Gamma_C^s \rightarrow \Gamma_C^m$ exists, which maps the points on the slave side of the boundary to the possible contact point on the master side. We then define the vector field of normal directions n^Φ :

$$n^\Phi : \Gamma_C^s \rightarrow \mathbb{S}^2, \quad n^\Phi(x) := \begin{cases} \frac{\Phi(x) - x}{|\Phi(x) - x|} & \text{if } \Phi(x) \neq x \text{ (no contact)} \\ n^s(x) & \text{otherwise} \end{cases} \quad (2)$$

The gap function $g : \mathbb{R}^3 \rightarrow \mathbb{R}$, $x \mapsto |\Phi(x) - x|$ then measures the width of the gap between the two bodies in the normal direction (i.e., aperture of the fracture in geophysics) and we also define the point-wise jump $[u] := (u^s - u^m \circ \Phi) \cdot n^\Phi$, which is to be smaller than the gap g , i.e. $[u] \leq g$. This condition is only meaningful in the linearized contact setting, where the bodies are close together and the outer normals n^α , $\alpha \in \{m, s\}$ are parallel, i.e. we have $n^s := n^\Phi$ and $n^m := -n^s$.

For the contact conditions we need stresses and displacements with respect to the outer normal direction and the tangential direction t :

$$\begin{aligned} \sigma_n^\alpha &= n_i^\alpha \cdot \sigma_{ij}(u^\alpha) \cdot n_j^\alpha, & u_n^\alpha &= u^\alpha \cdot n^\alpha, \\ \sigma_t^\alpha &= \sigma(u^\alpha) \cdot n^\alpha - \sigma_n^\alpha \cdot n^\alpha, & u_t^\alpha &= u^\alpha - u_n^\alpha \cdot n^\alpha. \end{aligned} \quad (3)$$

With this we state the contact problem in its strong form. We assume that the body is in an equilibrium state with body forces f (Eq. 4), Dirichlet boundary conditions (Eq. 5), Neumann boundary conditions with pressure p_i (Eq. 6) and contact boundary conditions (Eq. 7). As contact conditions we have the non-penetration condition 9, the complementary condition 10, and lastly Equation 11 which states that we have no stresses in tangential directions, i.e., we are considering frictionless contact:

$$-\text{div } \sigma(u) = f \quad \text{in } \Omega^s \cup \Omega^m \quad (4)$$

$$u_i = 0 \quad \text{on } \Gamma_D^\alpha \quad (5)$$

$$\sigma_{ij}(u) \cdot n_j = p_i \quad \text{on } \Gamma_N^\alpha \quad (6)$$

$$\sigma_n \leq 0 \quad \text{on } \Gamma_C. \quad (7)$$

$$\sigma_n(u^m \circ \Phi) = \sigma_n(u^s) \quad \text{on } \Gamma_C^s \quad (8)$$

$$[u] \leq g \quad \text{on } \Gamma_C^s \quad (9)$$

$$([u] - g)\sigma_n(u^s) = 0 \quad \text{on } \Gamma_C^s \quad (10)$$

$$\sigma_T = 0 \quad \text{on } \Gamma_C. \quad (11)$$

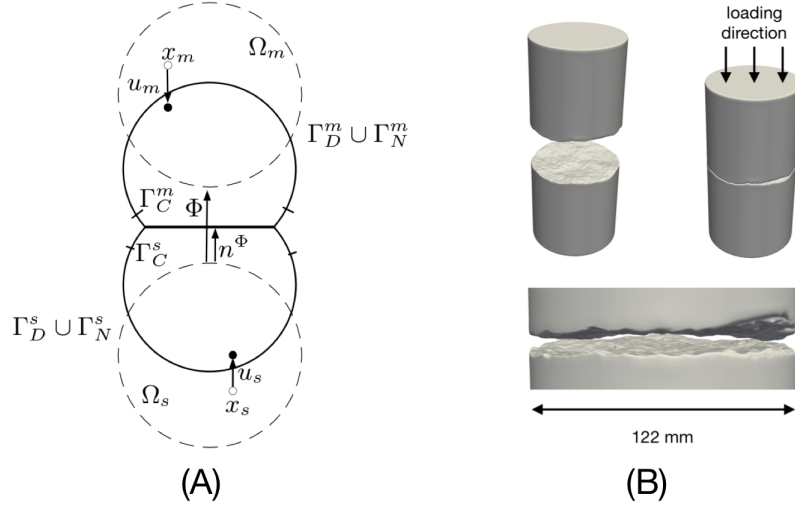


Figure 2: Two-body problem: A) Schematic of the contact problem between two spheres. The dotted lines indicate the initial position of the bodies, the solid lines show the contact configuration. B) Two-body problem for rough rock fractures. Two rock cylinders in open configuration (left), in closed configuration (right), and a close-up of the rough contact zone (bottom).

For the weak formulation we use the space $X := X(\Omega^m) \times X(\Omega^s)$, where $X(\Omega^\alpha) = [H_0^1(\Omega^\alpha)]^3$, $\alpha \in \{m, s\}$ are the usual Sobolev spaces, satisfying the Dirichlet boundary conditions (Eq. 5) and we define the bilinear form $a(u, v)$:

$$a(u, v) := \sum_{\alpha \in \{m, s\}} \int_{\Omega^\alpha} E_{ijkl}^\alpha u_{k,j} v_{l,m} dx \quad w, v \in X, \quad (12)$$

and the linear functional $\mathcal{U}(v) := \int_{\Omega} f v dw + \int_{\Gamma_n} p v d\gamma$. Furthermore, we introduce the convex set of admissible displacements $\mathcal{K} \subset X$:

$$\mathcal{K} := \{u \in X \mid [u] \leq g, \text{ a.e. on } \Gamma_C^s\}. \quad (13)$$

Here the inequality needs to be interpreted pointwise. We can now state the contact problem in its weak form as the minimum of the energy functional $J(u) := \frac{1}{2}a(u, u) - f(u)$: Find a $u \in \mathcal{K}$ such that:

$$J(u) \leq J(v), \quad \forall v \in \mathcal{K}. \quad (14)$$

We end this subsection by introducing the finite element spaces $X_h := X_h(\Omega^m) \times X_h(\Omega^s)$ associated to X and appropriate triangulations \mathcal{T}_h^m and \mathcal{T}_h^s of Ω^m and Ω^s with mesh width h . Using the basis functions ϕ_i of X_h we define

$$\mathbf{A} := a(\phi_i e_k, \phi_j e_l) \text{ and } \mathbf{f} := \mathcal{U}(\phi_i e_k), \quad i, j = 1, \dots, N; k, l = 1, \dots, 3, \quad (15)$$

where N is the number of nodes of the meshes $\mathcal{T}_h^\alpha, \alpha \in \{m, s\}$ and $(e_i)_{i=1,2,3}$ are the standard basis vectors in \mathbb{R}^3 . $\mathbf{A} \in \mathbb{R}^{3N \times 3N}$ is usually referred to as the stiffness matrix and $\mathbf{f} \in \mathbb{R}^{3N}$ as the right-hand side in the FEM context. The following subsections show, how the discretized system is solved by applying a change of basis on \mathbf{A} which includes a mortar projection. A weak and discretized version \mathbf{g} of g is obtained as a byproduct of the computation of the mortar projection routine.

2.2 Dual Mortar Approach

For the description of the dual mortar approach we follow [22, 12]. We remind the reader, that in one of the earlier papers on the Mortar method [7], the method was originally a domain decomposition method. Motivated by the need to solve partial differential equations on a domain with different non overlapping and non matching triangulations, the idea is essentially to "stitch" together the solution across the domain by enforcing a weak equality on the boundary of the two triangulations. Using our notation from the previous section, this implies $g = 0$, and solving a linear elastic problem on the domain $\Omega = \Omega^m \cup \Omega^s$ under the condition

$$\int_{\Gamma_C^s} [u] \tilde{\mu} d\gamma = 0, \tilde{\mu} \in \tilde{M}, \quad (16)$$

where \tilde{M} is a modified trace space on the boundary of two different triangulations.

The dual mortar method we use here, differs from this original setting in three ways. First, we consider bodies which might initially not be in contact, i.e. $g \neq 0$. Second, in order to allow the bodies to separate from each other, the equality condition in Eq. 16 becomes an inequality condition (see [6]). And lastly, for the Lagrange multipliers we consider the convex cone M^+ defined as

$$M^+ = \left\{ \mu \in M \mid \int_{\Gamma_C^s} \mu \lambda_+^s d\gamma \geq 0, \forall \lambda_+^s \in X(\Gamma_C^s)^+ \right\}, \quad (17)$$

where $X(\Gamma_C^s)$ denotes trace space of $X(\Omega^s)$ on the boundary Γ_C^s , M the dual of $X(\Gamma_C^s)$ and $X(\Gamma_C^s)^+ := \{\lambda_+^s \in X(\Gamma_C^s), \lambda_+^s \cdot n^s \geq 0\}$. We can then replace the strong non-penetration condition in Equation 9 in such a way, that we only allow for penetration in the normal direction in a weak sense:

$$\int_{\Gamma_C^s} ([u] - g) \mu \cdot n^s d\gamma \leq 0, \mu \in M^+. \quad (18)$$

In practice the weak non-penetration condition is difficult to enforce. Not only might the elements u^s and u^m initially be apart, even when the two bodies are in contact, i.e. $g = 0$, the nodes on the surface triangulations are non matching. Thus, to relate the nodes of the master side to the slave side of the contact boundary, an additional operator is needed - our mortar projection Ψ .

The construction of Ψ is then deduced in "reverse" by assuming the previously introduced mapping Φ , which is part of the solution, already exists. To do so, we introduce the discrete trace spaces $X_h(\Gamma_C^m)$ and $X_h(\Gamma_C^s)$ of $X_h(\Omega^m)$ and $X_h(\Omega^s)$. For one coordinate they are spanned by the bases $(\lambda_i^m)_{i=1, \dots, N^m}$, $(\lambda_i^s)_{i=1, \dots, N^s}$ with dimension N^m and N^s . M_h^+ denotes the set of the normal parts of the discrete variant of M^+ and is spanned by biorthogonal basis functions μ_k with the same dimension as

$X_h(\Gamma_C^s)$, i.e. $k = 1, \dots, N^s$. They get their name from the biorthogonality condition they fulfill, which, by using δ_{ik} as the Kronecker symbol, reads:

$$\int_{\Gamma_C^s} \mu_k \lambda_i^s d\gamma = \delta_{ik} \int_{\Gamma_C^s} \lambda_i^s d\gamma. \quad (19)$$

We then demand that for the mortar projection $\Psi : \Gamma_C^s \rightarrow \Gamma_C^s$ and the multiplier space M_h , the following weak equality holds for all elements $u_h^m \circ \Phi \in X_h(\Gamma_C^s)$:

$$\int_{\Gamma_C^s} (\Psi(u_h^m \circ \Phi) - u_h^m \circ \Phi) \mu_h d\gamma = 0, \quad \forall \mu_h \in M_h^+. \quad (20)$$

To get a discrete representation \mathbf{T} of Ψ , we write the elements $u_h^m \circ \Phi$, $\Psi(u_h^m \circ \Phi)$ and μ_h in the basis representations $u_h^m \circ \Phi = \sum_{i=1, \dots, N^m} v_i (\lambda_i^m \circ \Phi)$, $\Psi(u_h^m \circ \Phi) = \sum_{j=1, \dots, N^s} w_j \lambda_j^s$, $\mu_h = \sum_{k=1, \dots, N^s} l_k \mu_k$, and reformulate Equation 20 to:

$$\sum_{i=1, \dots, N^m} v_i \int_{\Gamma_C^s} (\lambda_i^m \circ \Phi) \mu_k d\gamma = \sum_{j=1, \dots, N^s} w_j \int_{\Gamma_C^s} \lambda_j^s \mu_k d\gamma, \quad \forall k = 1, \dots, N^s. \quad (21)$$

We now define $\mathbf{D} := (d_{ki})_{k,i=1, \dots, N^s}$ and $\mathbf{B} := (b_{kj})_{k=1, \dots, N^m, j=1, \dots, N^s}$ through:

$$d_{ki} := \int_{\Gamma_C^s} \lambda_i^s \mu_k d\gamma Id \quad \text{and} \quad (22)$$

$$b_{kj} := \int_{\Gamma_C^s} (\lambda_j^m \circ \Phi) \mu_k d\gamma Id, \quad (23)$$

where $Id \in \mathbb{R}^{3 \times 3}$ is the identity operator. We then reformulate Equation 21 with $\mathbf{v} = (v_i)_{i=1, \dots, N^m}$ and $\mathbf{w} = (w_j)_{j=1, \dots, N^s}$ as

$$\mathbf{B}\mathbf{v} = \mathbf{D}\mathbf{w}, \quad (24)$$

and with $\mathbf{T} := \mathbf{D}^{-1}\mathbf{B}$, we get the discrete representation of the mortar transfer operator. Its purpose is to represent elements of u_h^m of $X_h(\Gamma_C^m)$ via Φ in $X_h(\Gamma_C^s)$ in a meaningful way, using the weak equality in Equation 20. Computing the possibly dense inverse \mathbf{D}^{-1} could potentially add additional computational complexity, but due to our specific choice of M_h and condition Eq.19, \mathbf{D} becomes an easily invertible diagonal matrix. With \mathbf{T} it is now possible to formulate the non-penetration condition (compare Eq. 9) in its discrete form at each node p on the slave side Γ_C^s :

$$((u_h^s)_p - (\mathbf{T}u_h^m)_p) \cdot \mathbf{n}_p^s - g_p \leq 0, \quad p = 1, \dots, N^s. \quad (25)$$

Where $(u_h^s)_p, (u_h^m)_p \in \mathbb{R}^3$ denote local nodal vectors at node p , \mathbf{n}_p^s the normal vector at node p , and $\mathbf{g} = (g_p)_{p=1, \dots, N^s}$ is the weighted gap vector defined as:

$$g_p := (D^{-1}g')_p, \quad (g')_p := \left(\int_{\Gamma_C^s} \mu_p g d\gamma \right) \mathbf{n}_p^s, \quad p = 1, \dots, N^s. \quad (26)$$

Computing the entries d_{ki} and b_{kj} , which are surface integrals on a trace space, is nontrivial: Apart from computing an approximation to Φ , one needs to find suitable quadrature points on $\text{supp}(\lambda_i^s) \cap \text{supp}(\lambda_j^m \circ \Phi)$, which is especially tedious in cluster computing when the meshes \mathcal{T}_h^s and \mathcal{T}_h^m are distributed across several compute nodes. We use the library MOONoLith to obtain the quadrature points, as well as approximations to Φ , n^Φ and g , and we refer to [12] and [24] for an in-depth description of the required procedures, i.e. detection of intersections between the non matching meshes, load distribution and parallel communication.

2.2.1 Remark

By defining the bilinear form $b : H_0^{-1/2}(\Gamma_C^s) \times X(\Gamma_C^s) \rightarrow \mathbb{R}$, $b(\mu, v) := \langle \mu, [v] \rangle$, where $\langle \cdot, \cdot \rangle$ denotes the dual pairing, the contact problem can be formulated as a saddle point problem. Find $(\mu, u) \in M_h^+ \times X_h$ such that:

$$a(u_h, v_h) + b(\mu_h, v_h) = f(v_h), \quad \forall v_h \in X_h, \quad (27)$$

$$b(\mu_h, u_h) \leq \langle \mu_h, g \rangle, \quad \forall \mu_h \in M_h^+. \quad (28)$$

One can show that a uniform inf-sup condition holds and under additional mild assumptions the following a-priori error estimate between the discrete solution (μ_h, u_h) and the real solution (λ, u) can be proven:

$$\|u - u_h\| + \|\mu - \mu_h\|_{H^{-\frac{1}{2}}(\Gamma_C^s)} \leq C h^{\frac{1}{2} + \alpha} \sum_{k \in s, m} |u^k|_{\mathbf{H}^{\frac{3}{2} + \alpha}(\Omega^k)}, \quad \forall \alpha \in (0, \frac{1}{2}), \quad (29)$$

with $u^k \in \mathbf{H}^{\frac{3}{2} + \alpha}(\Omega^k) = [H^{\frac{3}{2} + \alpha}(\Omega^k)]^3$ (from [12], see also the references cited therein).

2.3 Algebraic formulation and solution

We apply an orthogonal transformation \mathbf{O} and a mortar transformation \mathbf{Z} on the assembled discrete finite element system. The orthogonal transformation was introduced by [21] and consists of Householder reflections at each contact node, whose purpose is to rotate the local coordinate systems at the nodes of the slave boundary Γ_C^s in the direction of the local normals and align it with the constrained direction. The matrix \mathbf{Z} algebraically transforms the two-body problem into a one-body problem (see remark 3.2 in [22]), thereby decoupling the non-penetration constraints $[u] \leq g$ (Eq. 9). Consequently we use \mathbf{u} for the coefficients of the solution vector in the standard basis and $\hat{\mathbf{u}}$ for the transformed basis. The solution is then be obtained from a quadratic optimization problem with $\hat{\mathbf{A}} := (\mathbf{OZ}) \mathbf{A} (\mathbf{OZ})^t$ and $\hat{\mathbf{f}} := (\mathbf{OZ}) \mathbf{f}_h$: Find a $\hat{\mathbf{u}}$, satisfying Eq. 25, such that

$$\frac{1}{2} \hat{\mathbf{u}}^t \hat{\mathbf{A}} \hat{\mathbf{u}} - \hat{\mathbf{f}}^t \hat{\mathbf{u}} \quad \text{is minimal.} \quad (30)$$

$$(31)$$

To construct \mathbf{O} and \mathbf{Z} , we label the nodes of the discretized finite element system with three index sets \mathcal{M}, \mathcal{S} and \mathcal{I} . The indices of the nodes on the boundary Γ_C^m on the master side are in \mathcal{M} , those at the slave side in \mathcal{S} and the indices of the remaining nodes in the interior are in \mathcal{I} . For the orthogonal transformation \mathbf{O} , we then use outer normals \mathbf{n}_i^s , $i \in \mathcal{S}$ at nodes of the slave side of the contact boundary to compute local householder transformations. These transform the local coordinate systems on the slave side of the contact boundary in such a way, that the first coordinate of each nodal vector points in the direction of the local normals:

$$\mathbb{R}^{3N \times 3N} \ni \mathbf{O} := o_{ij} = \begin{cases} \mathbf{id}_{3 \times 3} - \frac{2}{(\mathbf{n}_i^s)^t \mathbf{n}_i^s} \mathbf{n}_i^s (\mathbf{n}_i^s)^t & , i = j \text{ and } i \in \mathcal{S} \\ \mathbf{id}_{3 \times 3} & , i = j \text{ and } i \in \mathcal{I} \cup \mathcal{M} \\ 0 & , \textit{else.} \end{cases} \quad (32)$$

This has the effect that the constraints, introduced by the gap function g , only need to be considered on the first coordinate in each local coordinate system (see also [25, 21, 50]). Consequently, we assemble $\mathbf{g} \in \mathbf{R}^{3N}$ such, that we have the constraints

$(g_i, \infty, \infty)^t$ for the coefficients $\hat{\mathbf{u}}_i \in \mathbb{R}^3$ on the slave nodes $i \in \mathcal{S}$, whereby ∞ signifies no constraint.

The second transformation \mathbf{Z} uses the mortar operator \mathbf{T} from the previous section and is formed in the following way:

$$\mathbf{Z} := \begin{bmatrix} \mathbf{Id}_{\mathcal{I}} & 0 & 0 \\ 0 & \mathbf{Id}_{\mathcal{M}} & \mathbf{T}^t \\ 0 & 0 & \mathbf{Id}_{\mathcal{S}} \end{bmatrix} \in \mathbb{R}^{3N \times 3N}. \quad (33)$$

The multiplication with Z transfers the displacements of the master nodes to the slave nodes and transforms the two-body problem into a one-body problem. To illustrate this, we apply the operator \mathbf{Z}^{-t} to the solution \mathbf{u} :

$$\begin{bmatrix} \mathbf{Id}_{\mathcal{I}} & 0 & 0 \\ 0 & \mathbf{Id}_{\mathcal{M}} & 0 \\ 0 & -\mathbf{T} & \mathbf{Id}_{\mathcal{S}} \end{bmatrix} \mathbf{u} = \begin{bmatrix} \mathbf{u}_{\mathcal{I}} \\ \mathbf{u}_{\mathcal{M}} \\ -\mathbf{T}\mathbf{u}_{\mathcal{M}} + \mathbf{u}_{\mathcal{S}} \end{bmatrix} = \begin{bmatrix} \hat{\mathbf{u}}_{\mathcal{I}} \\ \hat{\mathbf{u}}_{\mathcal{M}} \\ \hat{\mathbf{u}}_{\mathcal{S}} \end{bmatrix} =: \hat{\mathbf{u}} \in \mathbb{R}^{3N}. \quad (34)$$

The constraints of the transformed system are now only on the third component $\hat{\mathbf{u}}_{\mathcal{S}}$ of the transformed solution vector $\hat{\mathbf{u}}$ (compare also with Eq. 25).

The system can be solved with semismooth Newton methods [16], or, what is another appeal of this transformation, with monotone multigrid methods of optimal complexity [25, 22, 12]. Unfortunately Hertzian contact theory makes several assumptions that are not necessarily met when dealing with real complex surfaces: small strains, elastic material, absence of friction, a relatively small contact area, each body being in essence a half space and lastly, small strains, close proximity and continuous surfaces. To accommodate for this, we apply a non-smooth SQP method similar to [23] in which we add an outer loop to the solution process. The contact problem is then solved as a sequence of $k = 1, \dots, n_{\text{outer}}$ contact problems, where in each iteration we adjust for the new obstacle configuration, i.e. we recompute the gap, the normal field and the mortar operator (see Alg. 1 where we added the subscript k for all iteration dependent terms).

Algorithm 1 Non-smooth SQP method.

Initialize $k, \hat{\mathbf{u}}_0, \mathbf{O}_0, \mathbf{Z}_0, \mathbf{g}_0, \mathbf{A}, \mathbf{f}_0$

for $k = 0$ to n_{outer} **do**

Solve $\hat{\mathbf{u}}_{k+1} = \underset{\hat{\mathbf{u}}}{\text{argmin}} \frac{1}{2} \hat{\mathbf{u}}^t \hat{\mathbf{A}}_k \hat{\mathbf{u}} - \hat{\mathbf{f}}_k^t \hat{\mathbf{u}}$ with: $\hat{\mathbf{u}} \leq \mathbf{g}_k$

Move meshes by applying displacement $\mathbf{u}_{k+1} - \mathbf{u}_k: \mathcal{T}_k^\alpha \mapsto \mathcal{T}_{k+1}^\alpha, \alpha \in \{m, s\}$.

Recompute $\mathbf{O}_{k+1}, \mathbf{Z}_{k+1}, \mathbf{n}_{k+1}$, and \mathbf{g}_{k+1} for step $k + 1$.

end for

Note that we have chosen a fixed n_{outer} as stopping criterion, which was heuristically determined from solving the benchmark problem in section 3.1. Alternatively, one could also define a relative criteria such the norm of the step length, etc.

2.4 Implementation

Our implementation is based on the MOOSE framework [14] and MOONoLith [24]. In geophysical applications, MOONoLith is primarily used to compute transfer operators

between different, nonmatching triangulations (see for example [47, 46, 36]). Here it is used to compute the previously described matrices \mathbf{D} and \mathbf{B} of the mortar projection, as well as the gap \mathbf{g} and the local normals \mathbf{n} . All matrices and vectors are integrated in MOOSE using several custom made MOOSE components, in which we also carry out the transformations described in the previous sections. To solve variational inequalities, such as contact problems, we have augmented the MOOSE framework with a new executioner class for the non-smooth SQP method and added a set of dedicated solvers. These include semismooth Newton, projected (nonlinear) node-based Gauss-Seidel, and monotone multigrid, all of which are implemented as SNES solvers in PETSc [2]. The overview of the framework is shown in Fig.3, whereby the operators refer to Eqs.15,31, 32, 33. We have also included libMesh [19], PETSc and UTOPIA [52] in the figure, which were used to create the interfaces. The integration of our components into MOOSE can be considered deep in the sense, that while the interfaces were designed as MOOSE components, calls to libMesh objects and methods within MOOSE, as well as to PETSC structs and functions, were used throughout the implementation. We like to remark that these libraries were chosen in particular, because they are proven, suitable for parallel cluster computing and open source.

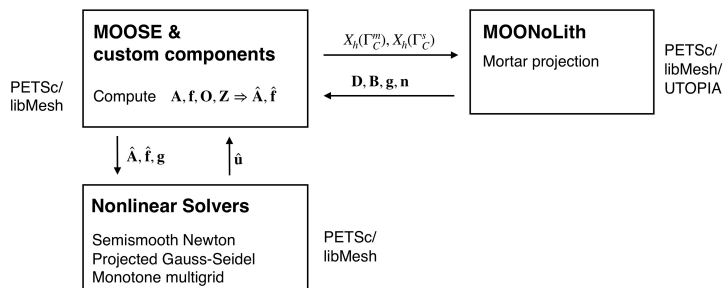


Figure 3

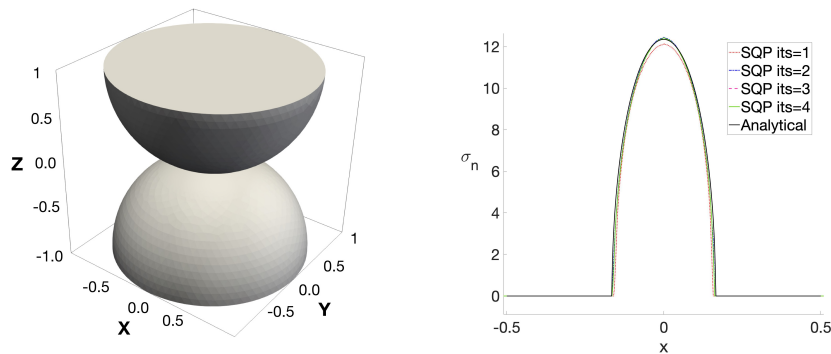
Figure 4: Schematic of the software components and their interaction.

3 Numerical experiments

3.1 Hertzian contact

To validate the method and to determine a reasonable number of SQP iterations, we set up a Hertzian contact problem. The term stems from a study by Heinrich Hertz in which he derived analytical solutions for two bodies in contact, which have elliptic contact interfaces [15]. In particular, in these kind of problems, one seeks to replicate the parabolic shape of the boundary stresses in the contact region. Here, we set up a two-body problem in which two half spheres are in contact (Fig. 5a). Both half spheres have radius 1, Youngs Modulus $E = 100$, Poisson ratio $\nu = 0.3$, and are moved into each other by a distance $d = 0.05$. The meshes of the two bodies have 330'379 nodes and are refined at the contact zones with a mesh width of roughly 5×10^{-5} . We then solve the Hertzian contact problem according to algorithm 1 with 1-4 SQP iterations.

To compare the results with the analytical solution, we infer the contact radius from the numerical result with 4 iterations and compute the boundary stresses analytically. The results are shown in Fig. 5b: The analytical solution is depicted as a solid black line. The solution after one SQP-iteration (dotted red line) deviates visibly from the analytical solution. After the second SQP iteration (blue line), the solution is almost congruent with the analytical solution and further improves slightly after three (dashed purple line) and four (solid green line) SQP iterations. As a consequence, we restricted ourselves to the use of three SQP iterations in the subsequent numerical experiments.



(a) Setup of the Hertzian contact problem, showing two half spheres in contact.

(b) Resulting contact stress distributions for several SQP iterations compared to analytical solution.

Figure 5: Hertzian Contact

3.2 Contact between two rough rock surfaces

The capability of the presented methodology to solve contact problems between highly complex surface topographies is demonstrated in a numerical experiment with a rock specimen taken from the Grimsel underground rock laboratory in Switzerland. The rock fracture geometries are adapted from previous studies [42, 40, 43] and are embedded in a cylindrical specimen, consisting of granodiorite rock (Fig. 1). Here, an increasing compressive load is applied to the specimen cylinder top in the axial direction (z-direction), while displacement in the z-direction is fixed to zero, with a Dirichlet boundary condition on the cylinder bottom. The diameter of the cylinder is 122mm and the material is defined to be linear elastic with a Youngs Modulus of $E = 10\text{MPa}$ and a Poisson ratio of $\nu = 0.33$. Fracture surfaces were digitized with photogrammetric techniques [44, 45, 43], which produce a mesh of triangular elements at the body surface. From the surface mesh, a volumetric mesh of tetrahedral elements can be generated for the solid bodies with the software TRELIS [10]. The upper body contains 101'637 nodes and the lower body contains 98'866 nodes, which results in 601'509 degrees of freedom for the simulation. The upper contact boundary consists of 8793 nodes, the lower one has 7898 nodes. Since the meshes are non-uniform, these numbers are difficult to relate to a resolution, which is by definition a measure that only applies to uniform meshes. We would argue, however, that non-uniformness gives

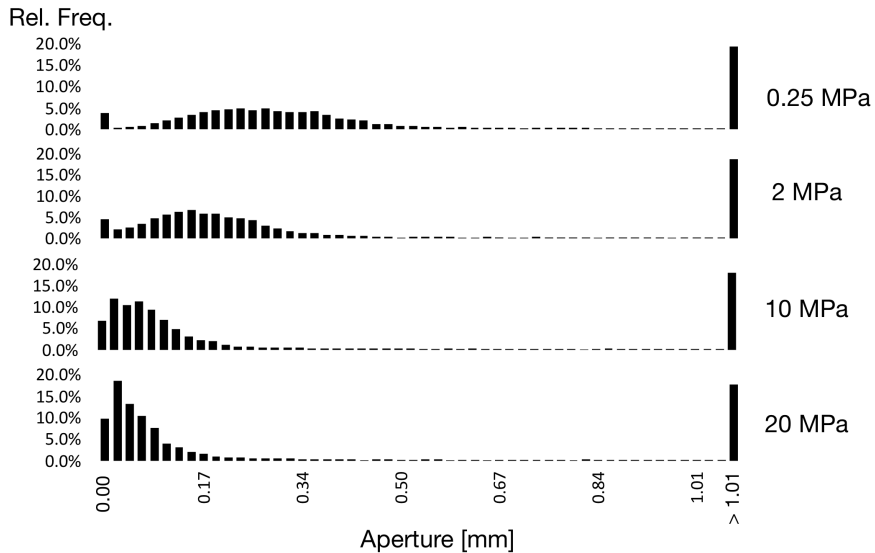


Figure 6: Histograms of the aperture distribution at increasing confining stresses of 0.25, 2, 10 and 20 MPa. As the confining stress increases, areas with large apertures become less frequent, while the frequency of small-aperture regions increases.

us at least the same, or even a higher, "effective" resolution as a uniform mesh, since the nodes are distributed more effectively in our case, as they are distributed according to the complexity of the rock surface (see Figure 1). The simulations themselves ran on 4 nodes (2 x Intel Xeon E5-2650 v3 @ 2.30GHz) with 10 CPU's each, on the cluster of the Institute of Computational Science in Lugano, Switzerland.

In this section, aperture is defined as the values of the gap function g , which reside on the nodes of the slave side. In its implementation, g differs from theory, as on a finite element mesh, normals are defined on the surfaces of the element sides and not at the nodes. The direction of g is therefore computed as the average of the normals of all sides of the mesh surrounding each node of the contact side. Still, we believe this to be a more accurate description of the distance between the fracture surfaces than a simple projection in the normal $(0, 0, -1)^t$ -direction and we thus use the value of g as aperture. For the assembly of the mortar operator, only intersections up to a reasonable distance of 0.21 mm are detected and the maximum value of the aperture is fixed at 0.21 mm. This does not impact the accuracy of the contact method, as the displacements of the rock are smaller than this maximum value (compare also with Figure 11).

Figure 7 shows the closure of the fracture aperture field under increasing normal loads, from 0.25 to 20 MPa. The aperture field is highly heterogeneous across the interface, with isolated regions of small apertures, for example, right of the center of the surface. Increasing the confining stress transforms the field significantly: At 0.25 MPa, only few parts of the surface are in contact and the apertures across large

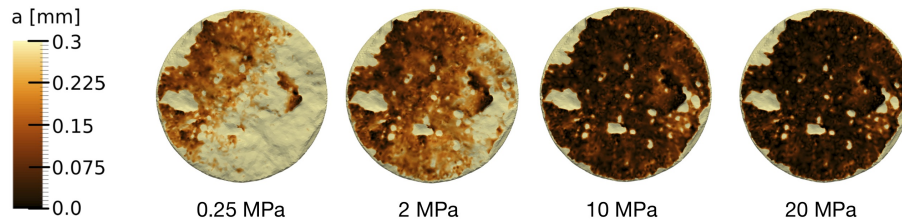


Figure 7: View of the different aperture fields under increasing confining stresses of 0.25, 2, 10 and 20 MPa.

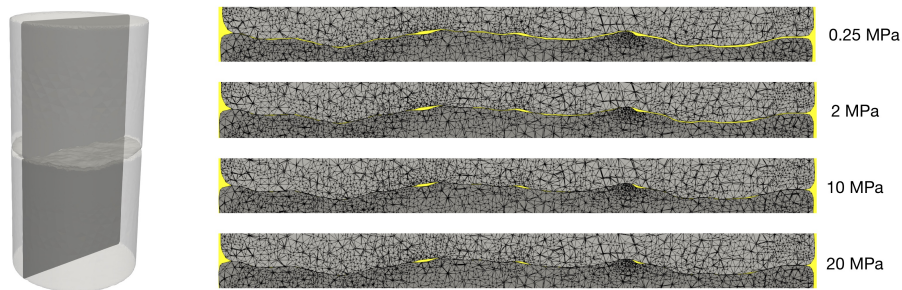


Figure 8: Left: 3D representation of the approximately horizontal fracture. Right: 2D view of the fracture, shown on the left. Open regions of the fracture are shown in yellow.

parts of the surface are at the maximum value of 0.21 mm. The aperture field then decreases significantly for a confining stress of 2 MPa and even more so at 10 MPa. There are regions, however, which do not close, so that apertures of at least 0.21 mm remain, even when the confining stress is further increased to 20 MPa. The closing of the fracture is again illustrated in Figure 8, where we show a cross section of the fracture during closure with the open part of the fracture depicted in yellow. At 0.25 MPa, there are only few contact areas and a large part of the fracture is still open. One can observe how the fracture closes more and more with increasing normal stress until, at 20 MPa, the only open areas are essentially those, where the fracture geometry indicates cavities. In Figure 6, we illustrate the overall behavior of the aperture field during closure. As the confining stress increases, the histogram is shifted to the left and the aperture field is distributed around a lower mean.

Hence, our method replicates the closure of the fracture in contact, free of over-closure. Studying the aperture field, the cross-section and the aperture histogram (Figure 7, 8, 6), we see that even at confining stresses of 10 and 20 MPa, the fracture is far from closed. Small cavities and channels still exist and the deformed fracture geometries can be used for simulating fluid flow under increasing confining stresses. The development of the vertical stresses is shown in Figure 9. The vertical stresses develop around the few existing contact points for an axial load of 0.25 MPa and spread over the contact surface when loads of more than 10 MPa are applied. Comparing

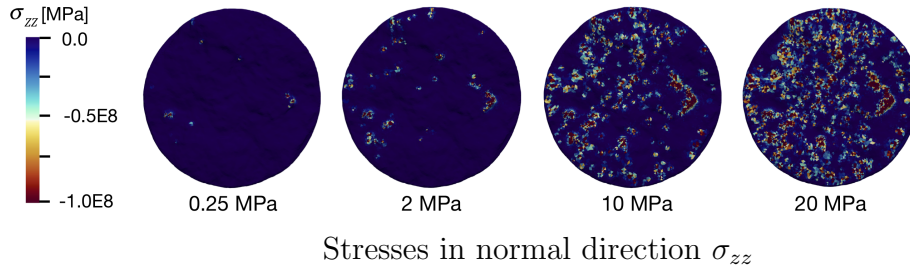


Figure 9: Top view of the lower fracture surface for confining stresses of 2, 10 and 20 MPa. The color indicates the vertical stresses σ_{zz} .

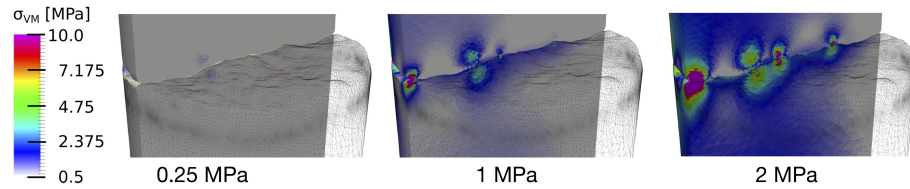


Figure 10: The color indicates von Mises stresses around contact points during the closure of the fracture at confining stresses of 0.25, 1 and 2 MPa.

Figures 7 and 9, we observe, that the first vertical stresses form around regions with small apertures (dark parts), which become more pronounced when the confining stresses are increased. In Figure 10, we show a cross section of the fracture with the von Mises stresses, developing at the contact nodes under increasing loads. In contrast to simpler contact models, we are able to observe, that the stresses develop from the contact surface in non-orthogonal directions in the interior of the body. This enables the observation of stress concentrations and stress shadows around contact regions.

While this study focuses primarily on contact detection, normal stresses, aperture field development and fracture closure, detailed knowledge of stress field variations around contact zones is of imminent importance. This is the case, as localized stress variations around zones of contact can lead to plastic deformation and failure, which permanently alter the mechanical and hydraulic behavior of the fracture [41]. The extent of stress concentrations around contact zones depends on both the external load as well as on fracture surface topographies. The presented approach therefore enables an estimation of stress extremes for fracture topographies commonly encountered in some specific rock types.

Rock fractures subjected to normal loading show a characteristic nonlinear fracture closure curve, where fracture closure becomes increasingly smaller for the same load increment, until it approaches the behavior of elastic deformation in a solid body [4, 27, 51, 41, 43, 20]. The fracture closure curve, obtained from our numerical experiment, is shown in Figure 11 for increasing axial loads from 0.25 to 20 MPa. Here, we increased the axial load incrementally in steps of 0.25 MPa from 0 to 2 MPa and then in steps

of 1 MPa from 2 to 20 MPa. The fracture closure (displacement) is measured as the average displacement of nodes in zones of about 1 mm thickness, approximately 2.5 cm above and 2.5 cm below the fracture. Displacement is measured at such a small distance from the fracture to avoid large heterogeneities in displacement due to the heterogeneous distribution of surface height and contact area over the entire fracture surface. To isolate displacements of the fracture, elastic displacements caused by the deformation in the lower specimen half, are excluded by subtracting the average displacements 2.5cm below the fracture from the average displacements 2.5cm above the fracture(see also [43]). The curve in Figure 11 shows, that the displacements become smaller when the confining stresses become larger, eventually leading to a linear relationship between axial load and displacement. The shape of the curve can be explained by noting that an increase in loading results in more areas of the fracture being in contact, increasing the overall resistance to the confining stress until a quasi-linear elastic response is reached. This is a well-known characteristics of loading curves and, together with the obtained boundary stresses for the Hertzian contact, underlines the soundness of our approach.

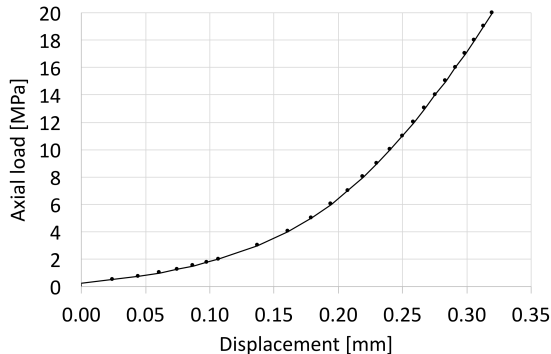


Figure 11: Simulated loading curve, showing displacement (i.e., fracture closure) versus axial load.

4 Conclusions

We implemented a dual mortar approach to compute the contact between two rough fracture surfaces with non-matching meshes, employing linear elasticity and linearized contact conditions. Unlike penalty methods, neither solution nor convergence depend on an external parameter and over-closure of the fracture is not a concern. To test our approach, we used complex fracture geometries, obtained from an actual granite rock. The high-resolution 3D fracture geometries were resolved from a rock specimen that had undergone laboratory experiments. We have demonstrated the validity of our method by reproducing the boundary stresses for Hertzian contact and the characteristic nonlinear closing behavior of a fracture under increasing normal loads. The presented methodology enables investigation of the stress field development and its variations in solid bodies, fracture aperture fields, contact areas and other behavior for arbitrary complex surface geometries.

Our implementation uses open-source software components that are designed for parallel computing. In particular, we use MOOSE for the finite element assembly and MOONolith for the computation of the mortar transfer operator. Together with our contact formulation, we can extend our framework to three directions: First, extend our formulation of frictionless contact to include friction as in [22, 32]. Second, use our formulation as a stepping stone for a wider class of more efficient multigrid obstacle solvers [22]. And third, leveraging our implementation in MOOSE, to simulate fluid flow with deforming fractures as a fluid-solid interaction approach, which we have outlined in [31].

Acknowledgements

We gratefully acknowledge funding by the Swiss Competence Center for Energy Research - Supply of Electricity (SCCER-SoE), by the Werner Siemens-Stiftung (Werner Siemens Foundation) and by ETH Zurich.

ORCID

C. von Planta - <https://orcid.org/0000-0002-3111-7186>
D. Vogler - <https://orcid.org/0000-0002-0974-9240>
P. Zulian - <https://orcid.org/0000-0002-5822-3288>
M.O. Saar - <https://orcid.org/0000-0002-4869-6452>
R.H. Krause - <https://orcid.org/0000-0001-5408-5271>

References

- [1] F. Amann, V. Gischig, K. Evans, J. Doetsch, R. Jalali, B. Valley, H. Krietsch, N. Dutler, L. Villiger, B. Brixel, M. Klepikova, A. Kittilä, C. Madonna, S. Wiemer, M. O. Saar, S. Loew, T. Driesner, H. Maurer, and D. Giardini. The seismo-hydromechanical behavior during deep geothermal reservoir stimulations: open questions tackled in a decameter-scale in situ stimulation experiment. *Solid Earth*, 9(1):115–137, 2018.
- [2] S. Balay, S. Abhyankar, M. F. Adams, J. Brown, P. Brune, K. Buschelman, L. Dalcin, V. Eijkhout, W. D. Gropp, D. Kaushik, M. G. Knepley, L. C. McInnes, K. Rupp, B. F. Smith, S. Zampini, H. Zhang, and H. Zhang. PETSc users manual. Technical Report ANL-95/11 - Revision 3.8, Argonne National Laboratory, 2017.
- [3] S. Balay, W. D. Gropp, L. C. McInnes, and B. F. Smith. Efficient management of parallelism in object oriented numerical software libraries. In E. Arge, A. M. Bruaset, and H. P. Langtangen, editors, *Modern Software Tools in Scientific Computing*, pages 163–202. Birkhäuser Press, 1997.
- [4] S. Bandis, A. Lumsden, and N. Barton. Fundamentals of rock joint deformation. *International Journal of Rock Mechanics and Mining Sciences & Geomechanics Abstracts*, 20(6):249 – 268, 1983.
- [5] F. B. Belgacem. The mortar finite element method with lagrange multipliers. *Numerische Mathematik*, 84(2):173–197, 1999.

- [6] F. B. Belgacem, P. Hild, and P. Laborde. The mortar finite element method for contact problems. *Mathematical and Computer Modelling*, 28(4-8):263–271, 1998.
- [7] C. Bernardi, Y. Maday, and A. T. Patera. Domain decomposition by the mortar element method. In *Asymptotic and numerical methods for partial differential equations with critical parameters*, pages 269–286. Springer, 1993.
- [8] F. Cappa and J. Rutqvist. Modeling of coupled deformation and permeability evolution during fault reactivation induced by deep underground injection of {CO₂}. *International Journal of Greenhouse Gas Control*, 5(2):336 – 346, 2011.
- [9] C. Co, D. Pollard, and R. Horne. Towards a better understanding of the impact of fracture roughness on permeability-stress relationships using first principles. 2017.
- [10] Computational Simulation Software LLC (csimsoft). Trelis meshing pre-processor. <https://www.csimsoft.com/trelis>, 2019. Online; accessed 01-April-2019.
- [11] B. Derode, F. Cappa, Y. Guglielmi, and J. Rutqvist. Coupled seismo-hydrromechanical monitoring of inelastic effects on injection-induced fracture permeability. *International Journal of Rock Mechanics and Mining Sciences*, 61:266–274, 2013.
- [12] T. Dickopf and R. Krause. Efficient simulation of multi-body contact problems on complex geometries: A flexible decomposition approach using constrained minimization. *International Journal for Numerical Methods in Engineering*, 77(13):1834–1862, 2009.
- [13] B. Figueiredo, C.-F. Tsang, J. Rutqvist, and A. Niemi. A study of changes in deep fractured rock permeability due to coupled hydro-mechanical effects. *International Journal of Rock Mechanics and Mining Sciences*, 79:70 – 85, 2015.
- [14] D. Gaston, C. Newman, G. Hansen, and D. Lebrun-Grandié. Moose: A parallel computational framework for coupled systems of nonlinear equations. *Nuclear Engineering and Design*, 239:1768–1778, 2009.
- [15] H. Hertz. Über die berührung fester elastischer körper. *Journal für die reine und angewandte Mathematik*, 92:156–171, 1882.
- [16] M. Hintermüller, K. Ito, and K. Kunisch. The primal-dual active set strategy as a semismooth newton method. *SIAM Journal on Optimization*, 13(3):865–888, 2002.
- [17] Y. Jiang, B. Li, and Y. Tanabashi. Estimating the relation between surface roughness and mechanical properties of rock joints. *International Journal of Rock Mechanics and Mining Sciences*, 43(6):837–846, 2006.
- [18] N. Kikuchi and J. T. Oden. *Contact problems in elasticity: a study of variational inequalities and finite element methods*. SIAM, 1988.
- [19] B. S. Kirk, J. W. Peterson, R. H. Stogner, and G. F. Carey. libmesh: a c++ library for parallel adaptive mesh refinement/ coarsening simulations. *Engineering with Computers*, 22:237–254, 2006.

- [20] T. Kling, D. Vogler, L. Pastewka, F. Amann, and P. Blum. Numerical simulations and validation of contact mechanics in a granodiorite fracture. *Rock Mechanics and Rock Engineering*, 51(9):2805–2824, 2018.
- [21] R. Kornhuber and R. Krause. Adaptive multigrid methods for signorini’s problem in linear elasticity. *Computing and Visualization in Science*, 4(1):9–20, 2001.
- [22] R. Krause. A nonsmooth multiscale method for solving frictional two-body contact problems in 2d and 3d with multigrid efficiency. *SIAM Journal on Scientific Computing*, 31(2):1399–1423, 2009.
- [23] R. Krause and C. Mohr. Level set based multi-scale methods for large deformation contact problems. *Applied Numerical Mathematics*, 61(4):428–442, 2011.
- [24] R. Krause and P. Zulian. A parallel approach to the variational transfer of discrete fields between arbitrarily distributed unstructured finite element meshes. *SIAM Journal on Scientific Computing*, 38(3):C307–C333, 2016.
- [25] R. H. Krause. *Monotone Multigrid Methods for Signorini’s Problem with Friction*. PhD thesis, Freie Universität Berlin, 2001.
- [26] J. Mao. A finite element approach to solve contact problems in geotechnical engineering. *International journal for numerical and analytical methods in geomechanics*, 29(5):525–550, 2005.
- [27] K. Matsuki, E. Wang, A. Giwelli, and K. Sakaguchi. Estimation of closure of a fracture under normal stress based on aperture data. *International Journal of Rock Mechanics and Mining Sciences*, 45(2):194 – 209, 2008.
- [28] M. W. McClure and R. N. Horne. Correlations between formation properties and induced seismicity during high pressure injection into granitic rock. *Engineering Geology*, 175:74 – 80, 2014.
- [29] K. Min, J. Lee, and O. Stephansson. Implications of thermally-induced fracture slip and permeability change on the long-term performance of a deep geological repository. *International Journal of Rock Mechanics and Mining Sciences*, 61:275–288, 2013.
- [30] K. Nemoto, N. Watanabe, N. Hirano, and N. Tsuchiya. Direct measurement of contact area and stress dependence of anisotropic flow through rock fracture with heterogeneous aperture distribution. *Earth and Planetary Science Letters*, 281(1-2):81–87, 2009.
- [31] C. Planta, D. Vogler, M. Nestola, P. Zulian, and R. Krause. Variational parallel information transfer between unstructured grids in geophysics-applications and solutions methods. *PROCEEDINGS, 43rd Workshop on Geothermal Reservoir Engineering, Stanford, CA*, pages 1–13, 2018.
- [32] A. Popp, B. I. Wohlmuth, M. W. Gee, and W. A. Wall. Dual quadratic mortar finite element methods for 3d finite deformation contact. *SIAM Journal on Scientific Computing*, 34(4):B421–B446, 2012.

- [33] L. J. Pyrak-Nolte and J. P. Morris. Single fractures under normal stress: The relation between fracture specific stiffness and fluid flow. *International Journal of Rock Mechanics and Mining Sciences*, 37(1-2):245–262, 2000.
- [34] E. Ritz, O. Mutlu, and D. D. Pollard. Integrating complementarity into the 2d displacement discontinuity boundary element method to model faults and fractures with frictional contact properties. *Computers & geosciences*, 45:304–312, 2012.
- [35] H. Sabetamal, M. Nazem, S. W. Sloan, and J. P. Carter. Frictionless contact formulation for dynamic analysis of nonlinear saturated porous media based on the mortar method. *International Journal for Numerical and Analytical Methods in Geomechanics*, 40(1):25–61, 2016.
- [36] P. Schädle, P. Zulian, D. Vogler, S. R. Bhopalam, M. G. Nestola, A. Ebigbo, R. Krause, and M. O. Saar. 3D non-conforming mesh model for flow in fractured porous media using Lagrange multipliers. *Computers & Geosciences*, 132:42–55, 2019.
- [37] B. S. A. Tatone and G. Grasselli. Characterization of the effect of normal load on the discontinuity morphology in direct shear specimens using x-ray micro-ct. *Acta Geotechnica*, 10(1):31–54, 2015.
- [38] J. W. Tester, B. Anderson, A. Batchelor, D. Blackwell, R. DiPippo, E. Drake, J. Garnish, B. Livesay, M. C. Moore, K. Nichols, et al. The future of geothermal energy: Impact of enhanced geothermal systems (egs) on the united states in the 21st century. *Massachusetts Institute of Technology*, 209, 2006.
- [39] R. Tian, M. Zhou, J. Wang, Y. Li, H. An, X. Xu, L. Wen, L. Wang, Q. Xu, J. Leng, et al. A challenging dam structural analysis: large-scale implicit thermo-mechanical coupled contact simulation on tianhe-ii. *Computational Mechanics*, pages 1–21, 2018.
- [40] D. Vogler. *Hydro-mechanically coupled processes in heterogeneous fractures: experiments and numerical simulations*. PhD thesis, ETH Zurich, 2016.
- [41] D. Vogler, F. Amann, P. Bayer, and D. Elsworth. Permeability evolution in natural fractures subject to cyclic loading and gouge formation. *Rock Mechanics and Rock Engineering*, 49(9):3463–3479, 2016.
- [42] D. Vogler, R. R. Settgast, C. Annavarapu, P. Bayer, and F. Amann. Hydro-mechanically coupled flow through heterogeneous fractures. *PROCEEDINGS, 42nd Workshop on Geothermal Reservoir Engineering, Stanford, CA*, SGP-TR-209:1–6, 2016b.
- [43] D. Vogler, R. R. Settgast, C. Annavarapu, C. Madonna, P. Bayer, and F. Amann. Experiments and simulations of fully hydro-mechanically coupled response of rough fractures exposed to high pressure fluid injection. *Journal of Geophysical Research: Solid Earth*, 123:1186–1200, 2018.
- [44] D. Vogler, S. D. C. Walsh, P. Bayer, and F. Amann. Comparison of surface properties in natural and artificially generated fractures in a crystalline rock. *Rock Mechanics and Rock Engineering*, 50(11):2891–2909, 2017.

- [45] D. Vogler, S. D. C. Walsh, E. Dombrowski, and M. A. Perras. A comparison of tensile failure in 3d-printed and natural sandstone. *Engineering Geology*, 226:221–235, 2017.
- [46] C. von Planta, V. D., X. Chen, M. Nestola, M. Saar, and R. Krause. Fluid-structure interaction with a parallel transfer operators to model hydro-mechanical processes in heterogeneous fractures and fracture intersections. submitted, 2019.
- [47] C. von Planta, V. D, X. Chen, M. Nestola, M. Saar, and R. Krause. Simulation of hydro-mechanically coupled processes in rough rock fractures using an immersed boundary method and variational transfer operators. *Computational Geosciences*, in press, 2019.
- [48] W. Wang, M. Zhou, B. Zhang, and C. Peng. A dual mortar contact method for porous media and its application to clay-core rockfill dams. *International Journal for Numerical and Analytical Methods in Geomechanics*, 2019.
- [49] B. I. Wohlmuth. A mortar finite element method using dual spaces for the lagrange multiplier. *SIAM journal on numerical analysis*, 38(3):989–1012, 2000.
- [50] B. I. Wohlmuth and R. H. Krause. Monotone multigrid methods on nonmatching grids for nonlinear multibody contact problems. *SIAM journal on scientific computing*, 25(1):324–347, 2003.
- [51] C. Zangerl, K. F. Evans, E. Eberhardt, and S. Loew. Normal stiffness of fractures in granitic rock: A compilation of laboratory and in-situ experiments. *International Journal of Rock Mechanics and Mining Sciences*, 45(8):1500–1507, 2008.
- [52] P. Zulian, A. Kopaničáková, M. C. G. Nestola, A. Fink, N. Fadel, V. Magri, T. Schneider, E. Botter, and J. Mankau. Utopia: A C++ embedded domain specific language for scientific computing. Git repository. <https://bitbucket.org/zulianp/utopia>, 2016.